Flow-seaweed interactions: A laboratory study using blade models

Davide Vettori[*][†], Vladimir Nikora

School of Engineering, University of Aberdeen, Aberdeen AB24 3UE, Scotland, UK
*Corresponding author. Email: d.vettori@lboro.ac.uk
†Current address: Department of Geography, Loughborough University, Loughborough, Leicestershire LE11 3TU, UK

Abstract

Flow-vegetation interactions is an interdisciplinary research area with applications in the management of coastal waters, lakes, and watercourses. Due to an emerging interest in the cultivation of seaweeds, this study seeks to develop a sound understanding of the physical interactions between flow and seaweeds. This is achieved via experiments in a laboratory flume using plastic-made models of blades of the seaweed species *Saccharina latissima*. In the experiments, strain gages, a digital camera, and Acoustic Doppler Velocimeters were used for measuring drag forces, blade movements (reconfiguration), and flow velocities. The study involved experiments with single blades and with pairs of tandem blades at different spacing between the blades. The revealed mechanisms controlling the dynamics of seaweed blade models varied depending on the ratio of blade length to eddy length scale. The drag coefficient of seaweed blade models appeared to be dependent on the Reynolds number, the Cauchy number, and the ratio of blade length to integral turbulence length scale. Turbulence had a primary role in controlling blade model dynamics and its drag coefficient. Seaweed blade models affected the flow in their wakes by increasing the turbulence intensity and reducing the mean longitudinal velocity. These effects on the flow are the reason for which, in a pair of tandem blades, the drag force experienced by the downstream blade is lower than that experienced by the upstream blade.

Keywords

Physical modelling; seaweeds; flow-vegetation interaction; turbulence; drag force; reconfiguration.

1. Introduction

The cultivation of seaweeds is expected to grow in the near future as a reflection of multiple potential applications which continue to rise (e.g. [28]). Over recent years, seaweeds have been explored for biofuel production (e.g. [23]), bioremediation (e.g. [14, 30]), and for development of Integrated

Multi-Trophic Aquaculture (IMTA) (e.g. [10, 11, 41]). A number of studies have also suggested that coastal vegetation may be used as an effective measure for wave attenuation and coastal defence (e.g. [38, 40, 49]). Nevertheless, seaweed aquaculture remains a very traditional sector, with techniques requiring a high amount of manual work, and is economically unsustainable in most developed countries [24]. For this reason, there is urgent need to develop novel techniques that minimise drag force acting on seaweed farms and maximise light and nutrients availability in order to make seaweed aquaculture economically more attractive. A multidisciplinary approach applied at a relevant range of spatial and temporal scales is therefore required (e.g. [33, 56]). Advancements in this field depend on the understanding of flow-seaweed interactions accounting for both physical and biological phenomena. Current knowledge of reciprocal interactions between drag force, reconfiguration, photosynthetic activity and nutrients uptake, however, remains incomplete and thus further research is needed.

Focusing on the physical aspects of the problem, most studies to date examined the mean values of drag force and flow velocity only, without fully characterising vegetation dynamics, while knowledge of the relationship between fluid flow and forces exerted on vegetation is fragmented [7]. In spite of recent efforts, the role of turbulence in vegetation dynamics remain poorly understood, and some works on flow-plant interactions highlight the existing inconsistencies [e.g. 7, 17, 22, 39, 46]. As an example, Huang et al. [22] and Rominger and Nepf [39] indicated that biomechanical properties are the primary factors in controlling seaweed dynamics, with ambient turbulence not showing correlation with seaweed reconfiguration. However, Cameron et al. [7] and Siniscalchi and Nikora [46] reported that dynamics of freshwater plants is mainly induced by ambient turbulence both in-situ and in laboratory flume. This discrepancy reflects the complexity of flow-plant interactions and motivates additional studies. Further, the authors are not aware of any work that appropriately quantified the effects of seaweed on the flow, essential to understand the seaweed-flow interactions and for some practical applications (e.g. wave attenuation).

The present study explores flow-seaweed interactions focusing on seaweed blade dynamics and the reciprocal interactions between ambient turbulence, drag force, and reconfiguration. This was achieved by conducting experiments in a laboratory flume with the use of physical models of seaweed blades. This approach was preferred to theoretical analyses, mathematical modelling, and field experiments due to its robustness and complementarity (e.g. [15, 16, 26]). When compared to experiments with live vegetation, the use of (abiotic) physical models is advantageous, as it provides complete control of the experimental conditions. Physical models do not require scrupulous care as live vegetation and can be manufactured with the desired features defined based on similarity considerations. On the other hand, physical models cannot reproduce the whole complexity of living organisms being a simplified replica of real plants (e.g. [16, 26]). Design and manufacture of physical models that consistently reproduce morphological and mechanical characteristics of real vegetation are highly challenging. For this reason, the present study focuses on the seaweed species *Saccharina latissima* that exhibits simple morphology making it easier to model. The morphological characteristics of *S. latissima* have been reported in Buck and Buchholz [6], and Spurkland and Iken [47]. *S. latissima* is characterised by a short stipe and a strap shaped blade, making it similar to a streamlined flag or ribbon (see Fig. 1c). Furthermore, *S. latissima* is widely distributed across the coasts of the North Atlantic, and is especially suitable for biofuel production (e.g. [57]) and IMTA (e.g. [41]), making it an appropriate species for this study.

In the present work we seek to develop a sound understanding of the physical mechanisms controlling the dynamics of single seaweed blades in a turbulent flow as well as the effects of the blades on the flow. In particular, we explore the role of turbulence in seaweed blade dynamics and the correlations between fluid flow, drag force acting on a seaweed blade, and its movements. In addition, pairs of seaweed blade models in a turbulent flow are also studied in order to understand how their interactions may affect the drag forces they experience. Section 2 describes the methods,

techniques, and instrumentation employed in this study. As our work is based on the experiments with physical models of seaweed blades, section 2 also contains the similarity considerations underpinning the design of the blade models. Section 3 reports the main results focusing on the drag forces acting on blade models, their reconfiguration, and their effects on the flow. In section 4 the main findings are discussed in order to provide a conceptual synthesis of the mechanisms controlling flow-seaweed interactions.

2. Materials and methods

2.1. Similarity considerations for seaweeds

In the study of flow-vegetation interactions, laboratory experiments are a useful tool for complementing field measurements and numerical models [50]. For the experiments to be representative of the natural processes we seek to reproduce, however, it is fundamental that all the relevant parameters are scaled correctly. In this study, we focus on single seaweed blades immersed in a unidirectional quasi-uniform turbulent flow. Waves and their effects on the seaweed blades are neglected, but this simplification does not compromise the research validity, as tide actions are dominant over waves in many sheltered marine locations (e.g. Scottish sea lochs). From an engineering perspective, the drag force experienced by seaweed blades is the most important factor to take into account. A dimensionless expression for the normalized drag force (i.e. drag coefficient C_d) is obtained through dimensional analysis (Eq. 1) using the following physical quantities: seaweed blade length (l), width (w), and thickness (t); mean (time-averaged) longitudinal velocity (U_{up}), turbulent kinetic energy (TKE), and integral turbulence length scale (L_u) of the approach flow ($L_u = U_{up}T_u$, where T_u is the integral time scale of the longitudinal velocity); gravity acceleration (g); kinematic viscosity (v) and density (ρ_w) of water; density (ρ_s) and Young's modulus (E_s) of seaweed material; and mean (time-averaged) drag force experienced by the seaweed blade (F_d).

The quantities listed above are combined in order to create the dimensionless parameters shown in Eqs. (2)-(7). The drag coefficient is defined according to a conventional (static) approach [48], using the wetted surface area of the sample as a reference area. The blade shape is presented by the blade slenderness (i.e. l/t), which is included in the Cauchy number C_y (as in [13]). The outcomes of the similarity analysis are summarised below:

Drag coefficient	$C_d = f(Re_l, Fr_l, C_y, T_i, l_r, \mu_{D-B})$	(1)
Blade Reynolds number	$Re_l = U_{up}l/v$	(2)
Blade Froude number	$Fr_l = U_{up}/\sqrt{gl}$	(3)
Cauchy number	$C_y = \rho_w U_{up}{}^2 l^3/(E_s t^3)$	(4)
Turbulence intensity	$T_i = \sqrt{2TKE/3}/U_{up}$	(5)
Lengths ratio	$l_r = l/L_u$	(6)
Forces ratio	$\mu_{D-B} = F_D/[(\rho_s - \rho_w)lwt]$	(7)

In order to conduct experiments in laboratory flumes as described in section 2.3, it is necessary to scale down seaweed blade models. Scale ratios for the physical governing parameters are calculated keeping the blade Reynolds number Re_l and Cauchy number C_y identical for both seaweed blades and their models. This choice is made because inertial, viscous, and elastic forces are expected to play major roles in flow-blade interactions, while the role of gravity (i.e. Froude number Fr_l) is

likely to be negligible. The turbulence intensity T_i is approximately the same in both open-channel flow and tidal flow (e.g. [51, 52]) and thus we may reasonably assume the approximate identity on this similarity number for both cases. The integral turbulence length scale L_u is characteristic of the laboratory flow size and cannot replicate values typical of tidal flows, thus requiring appropriate re-scaling the blade sizes. Finally, as seaweed is almost neutrally buoyant (e.g. [18, 19, 54]), the ratio of drag to buoyancy forces is typically very high and, therefore, forces ratio in Eq. (7) can be neglected.

Bearing in mind the above arguments, we derived the scale ratios for the controlling parameters starting with setting the length scale ratio (i.e. ratio of the blade model length to seaweed blade length). The reason for this is that the length of the seaweed blades represents a more restrictive factor than the flow velocity, due to limited flow depth and width in a flume and a requirement that the blade movements should not be restricted by the flow boundaries. Taking into account the dimensions of the laboratory flumes to be used for the experiments (section 2.3), the following scale ratios were obtained: 1:5 for any dimension of the physical models; 5:1 for the mean approach velocity of the flow; and 25:1 for Young's modulus of the material of which models are made. The ranges of model parameters derived from the above ratios are summarised in Table 1, together with the characteristics of real seaweed blades.

Table 1 Ranges of values of morphological and mechanical characteristics of physical models of seaweed blades manufactured for this study, based on the data available in the literature on blades of *S. latissima* and the scale ratios outlined in section 2.1. Scale ratios shown in Table 1 are the target values calculated following similarity considerations; note that due to technical limitations the characteristics of the manufactured models can slightly differ from those predicted using these ratios

	Physical models	Seaweed blades	Reference	Scale ratios
l (mm)	70 – 390	100 – 2500	Buck and Buchholz [6]	1:5
w (mm)	6.1 – 26.4	20 – 200	Buck and Buchholz [6]	1:5
t (mm)	0.07 – 0.28	0.8 – 1.5	Spurkland and Iken [47]	1:5
ρ_s (kg/m³)	819 – 1059	1092	Vettori and Nikora [54]	1:1
E_s (MPa)	78 – 319	9.9	Boller and Carrington [4]	25:1

2.2. Design and manufacturing of seaweed blade models
Seaweed blade models were designed following the scale ratios proposed in section 2.1 and accounting for the morphological and mechanical properties of *S. latissima* available in the literature. Buck and Buchholz [6] studied the morphological features of blades of *S. latissima* collected from the North Sea and provided data on blade length and width that are used in the present study (Table 1). Since no data on the seaweed blade thickness from the North Sea were available, the data of Spurkland and Iken [47], whose study was conducted in Alaska, were used as a reference (Table 1). No information on the thickness variation within the blade is found in the literature and therefore models were built with constant thickness. In terms of the plane configuration, the blades were approximated as elongated rectangles with smoothed isosceles triangles at the ends (Fig. 1d). All blade models were designed with a width to length ratio derived from the empirical regression equations reported in Buck and Buchholz (Figure 6A in [6]).

Polyethylene (PE) was chosen as the material for manufacturing the blade models, as its mechanical properties (e.g. [29]) are close to the target values (i.e. $\rho_s = 1092$ kg/m³, $E_s = 4.71$ MPa [54]). Our direct measurements of the density and Young's modulus of PE sheets used for making blade models are summarised in Table 2 [53]. The PE density and Young's modulus varied among PE sheets and therefore it was necessary to make direct measurements for each of them. For each PE sheet, 40 specimens 10 cm long and 1 cm wide were prepared. For each specimen, density was obtained from measurements of weight and volume, and Young's modulus was calculated as the

slope of stress-strain curve from tensile tests using a benchtop testing machine as described in Vettori and Nikora [54]. Table 2 also shows the key morphological characteristics of seaweed blade models used in the experiments and the ranges of blade Reynolds number and Cauchy number in the flume experiments.

Two groups of blade models were originally designed. In the first group, the blade length to thickness ratio was kept constant in such a way that the Cauchy number was constant as well (subject to variations in material density and Young's modulus). In the second group, the same PE sheet was used and only blade length (and width) varied. The groups were designed in order to examine the effects of the Cauchy number on blade model hydrodynamic performances. Models L1, L3, L4, L6, and L7 belong to the first group; models L2, L5, L8 and L9 belong to the second group. Since the results for all models showed the same patterns independently from the group to which they belonged, in this work blade models are sorted by blade length (Table 2).

Table 2 Summary of morphological and mechanical characteristics of seaweed blade models manufactured from five PE sheets. Once the length of a blade model was determined, its width was obtained using the empirical regression equations reported in Buck and Buchholz [6], and blade thickness was accepted to be equal to the PE sheets available. For each PE sheet, the density and Young's modulus of the material were estimated from measurements of volume and weight, and tensile tests conducted on 40 specimens. The ranges of blade Reynolds number and Cauchy number for each blade model are listed as well (they are computed using values of mean approach velocity shown in Table 3)

Blade model	l (mm)	w (mm)	t (mm)	ρ_s (kg/m³)	E_s (MPa)	Re_l	C_y
L1	70	6.1	0.07	1059	240	$(0.7\text{-}3.8)\times10^4$	$(0.4\text{-}12)\times10^2$
L2	90	7.3	0.12	935	205	$(1\text{-}5)\times10^4$	$(0.2\text{-}6.4)\times10^2$
L3	100	8.0	0.10	819	319	$(1\text{-}5.3)\times10^4$	$(0.3\text{-}8.9)\times10^2$
L4	120	9.3	0.12	935	205	$(1.3\text{-}6.6)\times10^4$	$(0.6\text{-}15)\times10^2$
L5	190	10.5	0.12	935	205	$(1.9\text{-}10)\times10^4$	$(2\text{-}58)\times10^2$
L6	210	11.4	0.21	856	78	$(2.3\text{-}11)\times10^4$	$(2\text{-}37)\times10^2$
L7	280	14.6	0.28	992	209	$(3.1\text{-}16)\times10^4$	$(0.6\text{-}15)\times10^2$
L8	290	15.1	0.12	935	205	$(3.2\text{-}16)\times10^4$	$(0.8\text{-}21)\times10^3$
L9	390	26.4	0.12	935	205	$(4.3\text{-}21)\times10^4$	$(2\text{-}51)\times10^3$

2.3. Facilities and experimental setup

The experiments were conducted in the Fluid Mechanics Laboratory of the University of Aberdeen (Scotland, UK). Two glass-sided tilting recirculating flumes were used, one for the experiments with single blade models, and the other for the experiments with pairs of blade models. All experiments were performed at quasi-uniform flow conditions, which were achieved by adjusting the flow rate, bed slope, and a weir at the end of the flume.

2.3.1. Experiments with single blade models

Two sets of experiments were performed with single blade models: (i) experiments focusing on the blade-flow interactions (Fig. 1a); and (ii) experiments for studying the effects of seaweed blade models on the wake behind the blades. Each experiment was run at a flow depth of 0.30 m, with flow velocities measured using two Acoustic Doppler Velocimeters (ADVs), and the drag force exerted by the flow on the blade model measured with a Drag Measurement Device (DMD, section 2.4). All measurements were recorded synchronously for a period of 10 minutes. The ADV sampling volumes were located 0.22 m above the channel bed, at the blade level. The first ADV was located 0.2 m upstream of the test sample clamped end (Fig. 1a).

In the experiments focusing on the blade-flow interactions, the second ADV was positioned 0.1 m downstream of the blade model free end, and a digital camera was used for recording blade movements in the vertical plane (Fig. 1a). The digital camera was mounted on a tripod next to the flume glass wall. When studying the effects of seaweed blade models on the wake flow velocities, the experiments were conducted with the second ADV located at 15 different positions from 0.01 m to 0.3 m downstream of the blade model free end. These positions were defined according to logarithmic spacing. No video recording was involved in this case.
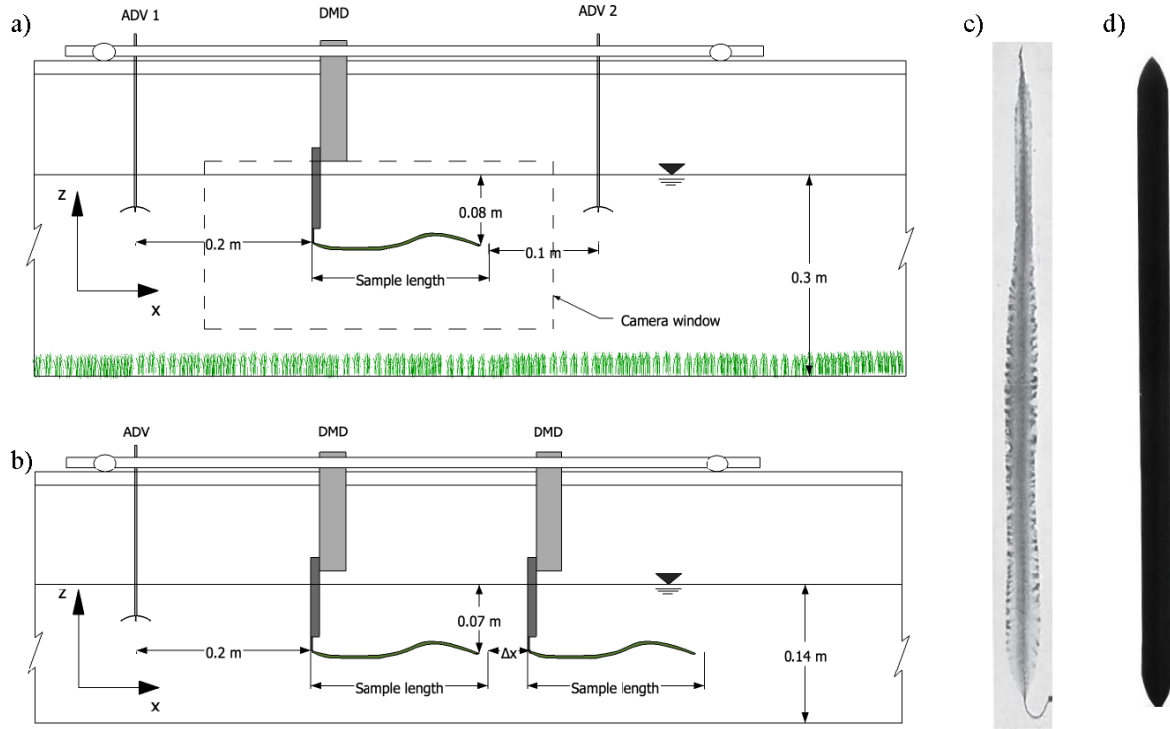

Fig. 1 (a) Experimental setup for studying single blade models (experiments on the blade-flow interactions; experiments focusing on the blade wakes had a similar set-up but with varying position of the downstream ADV). (b) Experimental setup for studying pairs of blade models. The ADVs and parts of the DMD were mounted on an instrumental carriage, with which they could be positioned at different locations across and along the flume. (c) Image of blade of *S. latissima* from an exposed site (adapted from Parke [35]). (d) Image of seaweed blade model used for laboratory experiments.

The experiments were performed in a 12.5 m long recirculating flume, with a rectangular cross-section 0.3 m wide and 0.45 m deep. In each experiment, a seaweed blade model was attached to the DMD and located in the central section of the flume, between 5.5 and 6.5 m from the inlet. To maximise the freedom of motion of the blade model, the water depth H was set to 0.3 m. The flume bed was covered with artificial grass (canopy height was 4.4 cm). Although the grass presence was not required for this study, it helped to maintain the level of turbulence intensity comparable to that in tidal flows (not too close to the bed), where longitudinal turbulence intensity typically ranges between 6% and 12% (e.g. [51, 52]). To identify the region within which the effects of the canopy and free surface were at minimum while vertical distribution of mean velocity and turbulent energy were quasi-homogeneous, a detailed set of ADV measurements was completed at multiple points along the vertical. Following these measurements, the vertical position of the blade model was selected to be at 0.22 m above the channel bed, where the vertical profiles of the turbulence quantities were quasi-homogeneous. In order to investigate a range of hydraulic conditions, each blade model was tested at seven flow scenarios (Table 3). All blade models shown in Table 2 were tested at these hydraulic conditions, with 63 experiments in total (i.e. 7 flow scenarios for 9 blade models).

2.3.2. Experiments with pairs of blade models

The experiments with pairs of blade models were conducted in a 11 m long, 0.4 m wide and 0.3 m high recirculating flume, at 6.5 m from the flume inlet to minimise the effects of inlet and outlet. The flume bed was fully covered with the stiff side of VELCRO and was hydraulically fully rough for both studied scenarios (Table 3). This flume was used to increase the flow width to provide more freedom for lateral blade motions. In each experiment, two seaweed blade models arranged in a tandem configuration (i.e. one upstream of the other) were attached to two DMDs, which individually recorded the drag forces experienced by the blade models. The downstream blade model was moved to different positions along the channel in order to investigate a range of separations between the blades. An ADV was positioned upstream of the blade models to measure the approach flow velocities. All instruments recorded synchronously for a period of 10 minutes. The water depth H was set to 0.14 m and the seaweed blade models and the ADV sampling volume were located 0.07 m above the channel bed, at the blades level. The selection of the flow depth of 0.14 m was driven by limitations of the flume design. Nevertheless, the background turbulence properties were largely similar to the experiments with single blades.

For logistical and timing reasons, the number of scenarios investigated for pairs of blade models was reduced compared to that performed with single blade models. Two seaweed blade models were selected among those shown in Table 2: blade model 'L1' and blade model 'L7'. In addition, only two flow scenarios were tested; they are described in Table 3 as 'Run 1P' and 'Run 2P'. Therefore, a total of 4 experiments (combinations of two flow scenarios and two blade models) were conducted.

Table 3 Hydraulic conditions used in the experiments with single blade models (from 'Run 1' to 'Run 7') and with pairs of blade models ('Run 1P' and 'Run 2P'). Note that U_{up} is the mean approach velocity measured in front of the blade model, while U_s is the cross-sectional averaged velocity

Flow scenario	Flow rate Q (m³/s)	H (m)	U_{up} (m/s)	U_s (m/s)	$Re = \dfrac{U_s H}{\nu}$
Run 1	7.0×10^{-3}	0.3	0.10	0.09	27,000
Run 2	11.8×10^{-3}	0.3	0.18	0.16	48,000
Run 3	16.6×10^{-3}	0.3	0.26	0.22	66,000
Run 4	21.5×10^{-3}	0.3	0.33	0.29	87,000
Run 5	26.4×10^{-3}	0.3	0.40	0.35	105,000
Run 6	31.2×10^{-3}	0.3	0.47	0.42	126,000
Run 7	26.0×10^{-3}	0.3	0.55	0.48	144,000
Run 1P	7.0×10^{-3}	0.14	0.15	0.13	18,200
Run 2P	20.5×10^{-3}	0.14	0.41	0.37	51,800

2.4. Instrumentation

The ADVs used during the experiments were '*Vectrino+*' manufactured by Nortek (Nortek AS, Rud, Norway), with the accuracy of 0.5% of flow velocity measurements [34]. The flow velocity vector is determined by ADV via measuring the Doppler shift induced by the moving particles in the fluid (e.g. [24]). The flow velocity vector is estimated in a sampling volume centred 5 cm below the acoustic transmitter for providing undisturbed measurements [34]. The height of the sampling volume was set to 9.2 mm and the sampling frequency to 100 Hz. The ADVs were controlled with a computer via dedicated software (*Vectrino Plus*, Nortek AS, Rud, Norway). The measured ADV data were conditioned (de-spiked) before performing statistical analysis (section 2.5).

The DMD employed during the experiments was an updated version of the instrument used by Albayrak et al. [1]. It was a custom-made device consisting of 1N SMD S100 thin film load cells (Strain Measurement Devices, Chedburgh, England) connected to a Vishay PG 6100 data acquisition

scanner (Vishay Precision Group, Malvern, USA) via 3 m long shielded cable (for experiments with single blade models single load cell was used, while for experiments with pairs of blade models two load cells were used synchronously). The scanner was controlled with a computer via dedicated software (*StrainSmart*, Vishay Precision Group, Malvern, USA). Each load cell was installed on an aluminium support so that it would detect only the force component parallel to the main flow (Fig. 2). The seaweed blade model was attached to a tapered copper rod that was connected to the free end of the load cell. The rod was inserted in a hydrofoil-shaped brass pipe to minimise its area exposed to the flow (Fig. 2). Strain Measurement Devices indicates the following properties for the load cells: resolution of 10^{-5} N, accuracy of 5×10^{-5} N, and maximum non-linearity of 5×10^{-5} N. Prior to an experiment, the load cells were calibrated using a series of weights of known values and a calibration relationship between the weight acting on the tip of the rod and the measured signal was obtained. The sampling frequency of the scanner was set to 200 Hz via *StrainSmart*. The ADVs and the DMD were synchronised via a high-voltage card installed in the data acquisition scanner and recorded for a period of 10 minutes.
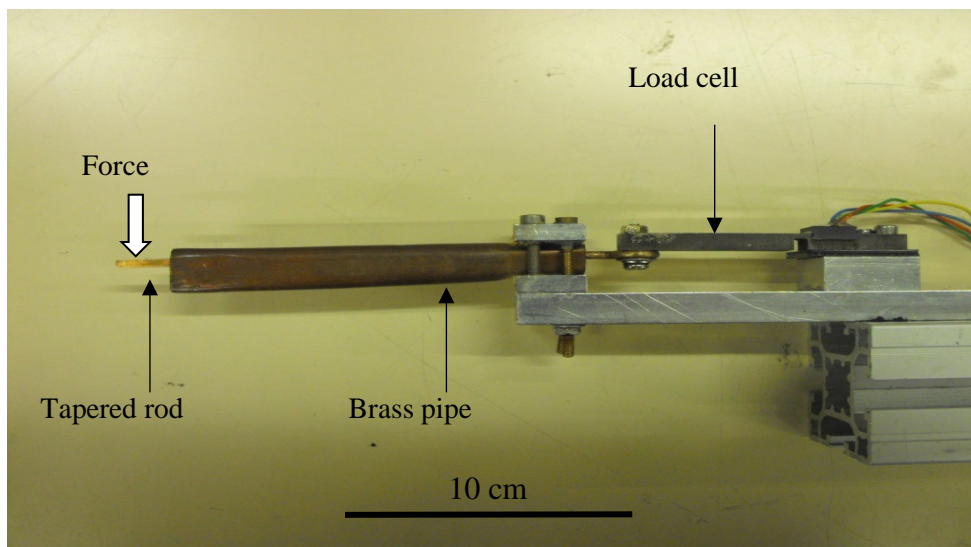

Fig. 2 Detail of the custom-made DMD displaying the tapered copper rod, protective brass pipe, and load cell mounted on the aluminium support. The tapered rod was connected to the load cell and mounted on the support so that it would not touch the protective pipe during the experiments

The digital camera used for recording the vertical movements of seaweed blade models was a Samsung HD HMX-R10BP (Samsung, Seoul, South Korea). The videos were recorded with HD resolution (i.e. 1920x1080 pixels) and with the maximum de-interlaced frequency of 25 Hz for 10 minutes.

2.5. Data analysis
The Doppler noise and signal aliasing affect the data collected with ADVs, with a consequent generation of erroneous spikes [20, 24, 32]. To remove them, a number of techniques have been developed, which consist of a despiking procedure and a replacement procedure (e.g. [9, 20, 25, 36]). In this study, raw velocity data collected with ADVs were despiked using the phase-space threshold method [20] modified as proposed by Parsheh et al. [36], with no pre-filtering. The amount of spurious data removed by this method was lower than 1% of the recorded data. The last good value approach was used in the replacement process [20].

Drag force data were processed via the data acquisition scanner with an A/D converter, which applied an automatic anti-aliasing low-pass FIR filter to the analogue signal, with a consequent delay of 0.025 s in the data. This delay was assumed to be negligible for the follow-up analysis. Due to the high sensitivity of the load cells, mechanical vibrations associated with the facility (i.e. pump, flume structure, and instrumental carriage) contaminated the measured drag force signal. Through a

preliminary analysis of the power spectral density functions $S_d(f)$ of the drag force, it was estimated that, in most experiments, more than 70% of the measured signal variance were associated with these vibrations. To overcome the problem, the drag force time series were filtered with a second low-pass FIR filter, which was designed by the authors and cut off the frequencies affected by the mechanical vibrations associated with the facility. The filtered drag force data were then used to calculate all relevant statistical quantities.

Videos recorded with the digital camera were processed with MATLAB® image processing tools. Each frame was converted to a black and white image and cropped so that only the objects relevant for image analysis were preserved. Then, the 'edge detection' method was employed to extract the vertical positions of the seaweed blade model by using the Canny edge detector algorithm [8]. This method identifies the areas with sharp changes in intensity within an image (i.e. edges), greatly reducing the amount of data to analyse [8]. After edge detection, each frame was divided in a number of vertical interrogation regions (strips) 10 pixels wide. A centroid was identified for each interrogation region as the mean of the vertical coordinates of all edges detected in that region (i.e. lower and upper edges of the seaweed blade model). Once the time series of the blade model vertical coordinates were obtained from the video analysis, they were corrected against the coordinate of the blade model clamped end and converted from the pixel coordinate system to the metric system. From the time series of the vertical position $z_b(\xi, t)$ of each centroid along the seaweed blade model (which can be assumed to be the vertical position of the blade model), the time series of the vertical velocity $w_b(\xi, t)$ of the blade model was estimated. Since the maximum excursion along blade models always occurred at their free end and power spectral density functions of blade vertical positions along the blade were self-similar, the blade model free end was selected as representative of the whole sample. The blade free end was subsequently used for conducting a comprehensive analysis of the blade reconfiguration using cross-correlations and power spectral density functions. Further details on the video processing techniques used in the study are reported in Vettori [53].

3. Results

3.1. Drag force experienced by single (isolated) blade models

As the mean flow velocity increases, the drag bulk statistics (i.e. mean value, standard deviation, skewness, and kurtosis) reveal the following patterns: (i) the mean drag force F_d has a positive trend $F_d \propto U_{up}^{2+\gamma}$, with values of Vogel's exponent γ [56] ranging from -0.6 to 0.2, where U_{up} is the mean approach velocity; (ii) the standard deviation σ_d significantly increases; (iii) the skewness remains close to 0, with no significant variations associated to changes in hydraulic conditions; and (iv) the kurtosis fluctuates insignificantly around 0. The drag standard deviation σ_d increases with the standard deviation σ_{u-up} of the approach flow velocity as $\sigma_d \propto \sigma_{u-up}^2$ (Fig. 3a).

The drag coefficient C_d was defined using the following equation [48]:

$$C_d = 2F_D / \left(\rho_w A_{wet} U_{up}^2 \right) \tag{8}$$

where A_{wet} is the wetted surface area of the seaweed blade model. The drag coefficient was investigated as a function of the most relevant dimensionless parameters introduced in section 2.1 (Eqs. 2, 4-6). It decreases significantly as l/L_u increases, following a decaying trend and with the highest values of C_d at $l/L_u < 1.0$ (Fig. 3b). The drag coefficient shows a clear dependence on Re_l (Fig. 3c), resembling the relationships reported for a flat plate in Schlichting and Gersten [42], i.e. a systematic decrease of C_d with increasing Re_l. However, its dependence on the Cauchy number C_y is different. The drag coefficient decreases up to $C_y \sim 10^3$ reaching a minimum at $C_y \sim 10^4$ and then showing a weak increase for higher values of the Cauchy number (Fig. 3d). The drag coefficient also

appears to be dependent upon the turbulence intensity T_i, increasing with increase in T_i (Fig. 3c). It is important to note that the two shortest blade models ('L1' and 'L2') exhibit different trends in relationships of C_d vs C_y and T_i, compared to other blade models.
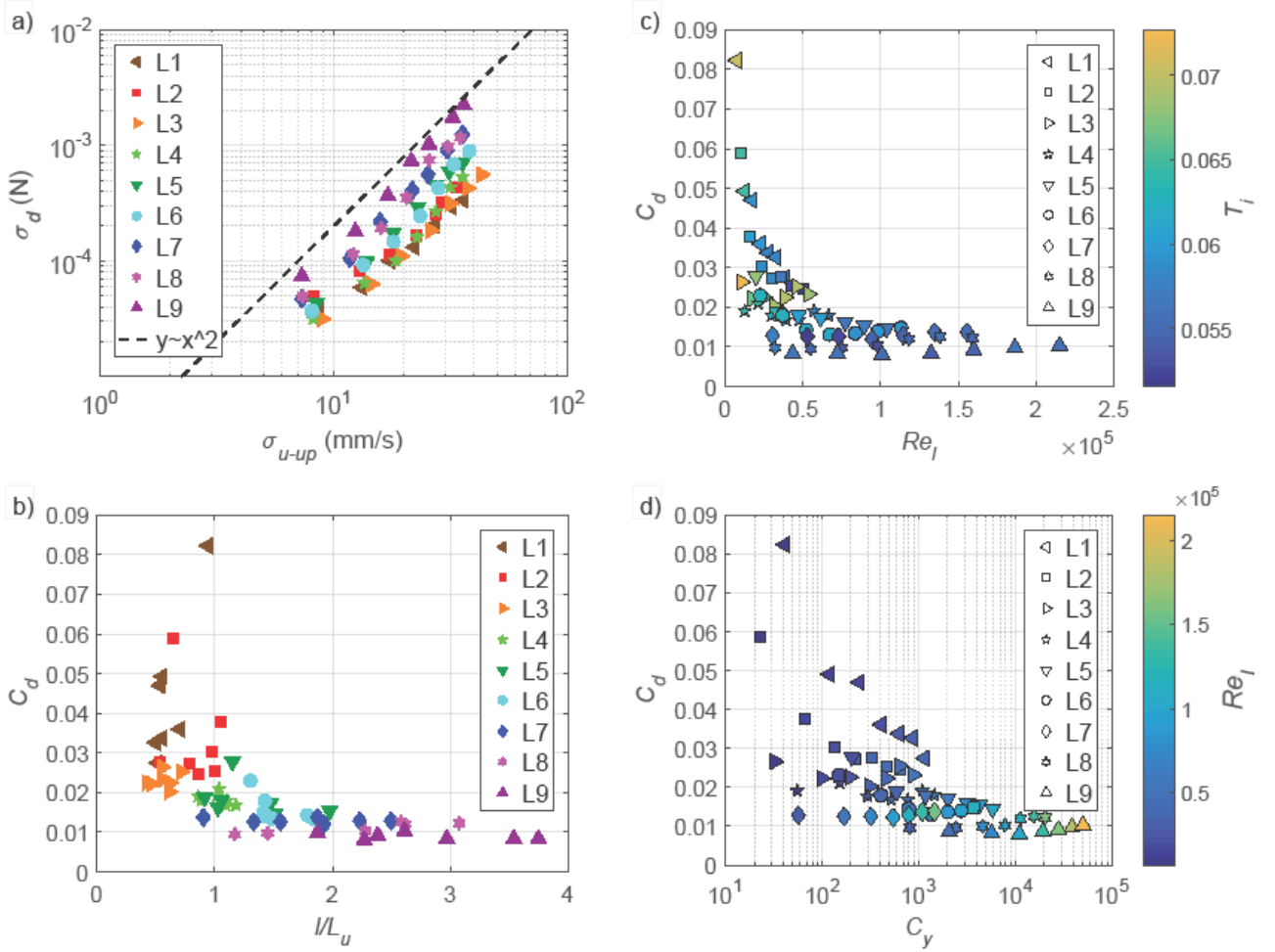

Fig. 3 (a) Standard deviation of the drag force experienced by seaweed blade models as a function of the standard deviation of the approach longitudinal velocity. (b) The drag coefficient of seaweed blade models as a function of the ratio of the blade length to the integral turbulence length scale (Eq. 6; $L_u = U_{up}T_u$, where T_u is the integral time scale of the longitudinal velocity). (c) The drag coefficient of seaweed blade models as a function of the blade Reynolds number (Eq. 2) and the turbulence intensity (Eq. 5). (d) The drag coefficient of seaweed blade models as a function of the Cauchy number (Eq. 4) and the blade Reynolds number (Eq. 2)

In the spectra of drag forces two main trends are noticeable: at low frequencies, a slope of - 1 in log-log coordinates is visible; then, as the frequency increases, the slope changes from -1 to -5/2. These patterns are clear in Fig. 4, which reports the drag spectra for two flow scenarios ('Run 1' and 'Run 5'). The -1 scaling region holds in the whole frequency domain for the two shortest seaweed blade models (i.e. 'L1' and 'L2') tested at flow scenarios characterised by low mean flow velocity (i.e. 'Run 1' and 'Run 2'). For other blade models, the high-frequency border of the -1 region moves to higher frequencies as the mean flow velocity increases. The most significant differences between $S_d(f)$ for different seaweed blade models are visible in the low frequency region, while with increase in frequency the spectra converge on the -5/2 scaling region, first reported for aquatic plants by Siniscalchi and Nikora [45]. Some apparently random peaks are also visible in the drag spectra (Fig. 4). They deviate from the background spectral trends and may reflect non-linear interaction between drag fluctuations and turbulence (Fig. 4). Their nature, however, remains unclear.
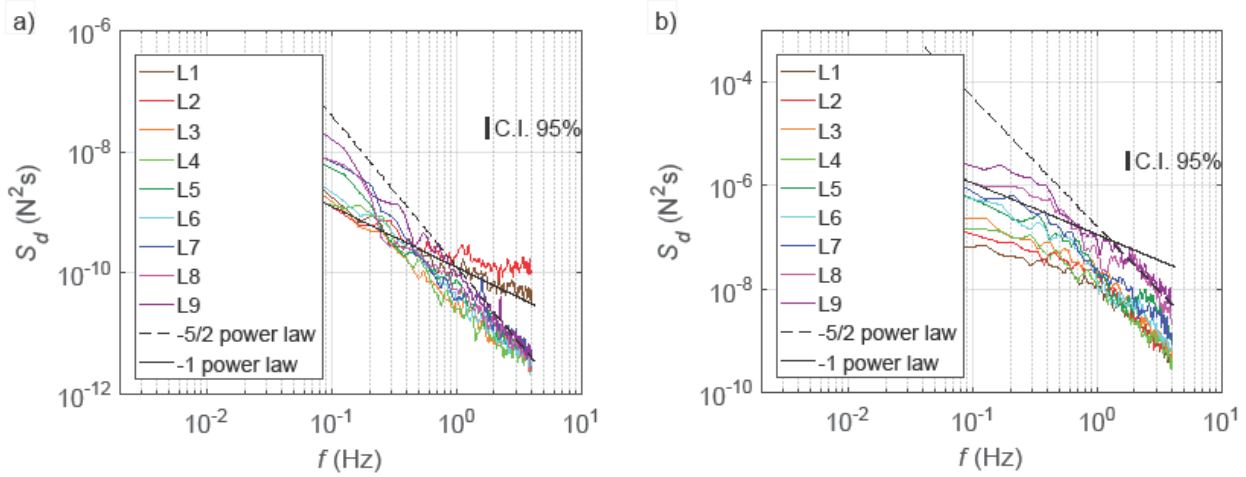
Fig. 4 The power spectral density functions of the drag force experienced by the seaweed blade models for flow scenarios 'Run 1' (a) and 'Run 5' (b). In both plots two slope lines (-5/2 and -1) are shown. The patterns displayed in (a) are representative of 'Run 1' and 'Run 2'; the patterns displayed in (b) are representative of the remaining flow scenarios. The black rectangle at the top right corner of the plots represents the 95% confidence interval for the spectral magnitudes [3]

3.2. Reconfiguration of single (isolated) blade models

The standard deviations of the vertical position σ_{zb} and vertical velocity σ_{wb} of seaweed blade models grow from the clamped end towards the free end, with σ_{wb} increasing linearly (Fig. 5a). The mean values of both seaweed blade model vertical position Z_b and vertical velocity W_b are very close to zero, meaning that the effects of buoyancy are negligible on the reconfiguration and the estimates of the vertical velocity are accurate, respectively. As the mean flow velocity increases from flow scenario 'Run 1' to 'Run 7', the following effects on the bulk statistics of the blade vertical velocity are noticeable: (i) W_b is always close to zero; (ii) σ_{wb} grows significantly along the blade model (Fig. 5a); (iii) the skewness is close to zero; and (iv) the kurtosis remains close to 1. The fact that the kurtosis is positive indicates that extreme positive fluctuations are present in the vertical velocity of seaweed blade models.

As indicated in section 2.5, a comprehensive analysis involving power spectral density functions and correlation functions was conducted using the vertical velocity at the free end of seaweed blade models. The obtained spectra $S_{wb}(f)$ of the blade vertical velocity can be divided into three regions: (i) a low frequency region where $S_{wb}(f)$ increases reaching a maximum; (ii) an intermediate frequency range where $S_{wb}(f)$ decreases as a power function with an exponent -4 (slope -4 in log-log coordinates); and (iii) a high frequency range where $S_{wb}(f)$ reaches the noise floor and, for low-flow scenarios, exhibits a second peak (Fig. 5b). This peak most likely relates to vortices shed from the blade models when the flow velocity is reasonably low. This effect is highlighted in section 3.3 and discussed in detail in section 4. As the mean flow velocity increases, the following effects are noticeable: (i) the maximum magnitude of $S_{wb}(f)$ grows, moving to higher frequencies and, consequently, shifting the -4 scaling region to the right as well (Fig. 5b); and (ii) the blade vertical velocity becomes less auto-correlated, i.e. the autocorrelation of vertical velocity crosses the zero at smaller time intervals.
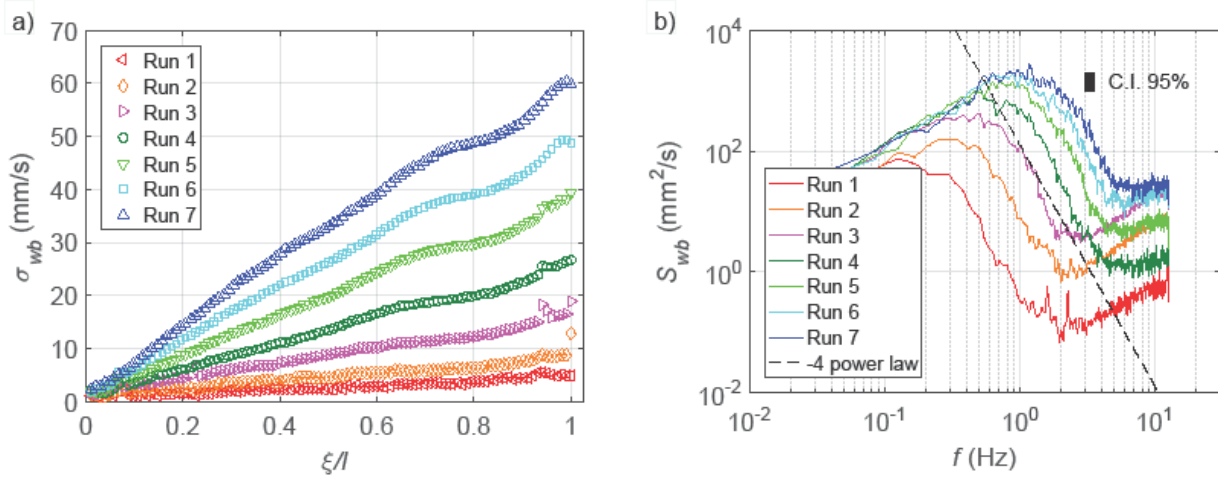
Fig. 5 (a) Standard deviations of the vertical velocity of seaweed blade model 'L7' (the position along the blade model ξ is normalised using the blade length l). (b) Power spectral density functions of the vertical velocity of seaweed blade model 'L7'. The -4 slope line is plotted in (b) as it well approximates the slope of $S_{wb}(f)$ in the intermediate frequency region. Both (a) and (b) display patterns that are representative of all blade models. The black rectangle at the top right corner of the (b) represents the 95% confidence interval

3.3. Effects of single (isolated) blade models on the flow

In order to investigate the effects of seaweed blade models on the flow, the characteristics of flow velocities upstream and downstream from the blades are compared. Prior to analysis, benchmark experiments were conducted to verify that: (i) the presence of the upstream ADV and the immersed parts of the DMD did not have significant influence on mean flow velocities or turbulence statistics; and (ii) the flow features identified were not generated by the facility, but were inherent to the presence of the blades. The data reveal that seaweed blade models alter the flow velocities downstream of their free end in the following ways: (i) the bulk statistics of the longitudinal velocity u_{ds} are significantly affected; (ii) the effects on the bulk statistics of the transverse velocity v_{ds} are negligible; and (iii) the bulk statistics of the vertical velocity w_{ds} are altered, but the effects are minor compared to those on the u_{ds} statistics. Therefore, this section is focused on the effects of seaweed blade models on the bulk statistics of the longitudinal velocity.

Within a distance of 10% of blade length l from the blade free end, the mean longitudinal velocity is reduced by up to 5-12% (Fig. 6a). As one would expect, the difference between the downstream mean velocity U_{ds} and the mean approach velocity U_{up} diminishes with increase in distance from the blade free end (Fig. 6a). In addition, the wakes behind seaweed blade models exhibit enhanced fluctuations of the longitudinal velocity. The standard deviation σ_u of the longitudinal velocity close to the blade free end is up to 80% higher than the corresponding value for the approach velocity (Fig. 6b). This increment is primarily associated with the presence of blade models rather than the submerged part of the DMD. Indeed, dedicated experiments showed that the immersed part of the DMD generates an increase in σ_u of up to 20% compared to σ_u of the approach velocity, i.e., its effect is much weaker compared to the blade effect. The variation of σ_u along the flow resembles that of the mean velocity: it remains constant within a distance of 10% l from the free end and then it reduces (Fig. 6b). Notably, variations in both mean and standard deviation of the longitudinal velocity reveal the similar general trends, roughly following a slope of -1/2 in log-log coordinates (Fig. 6a, b).
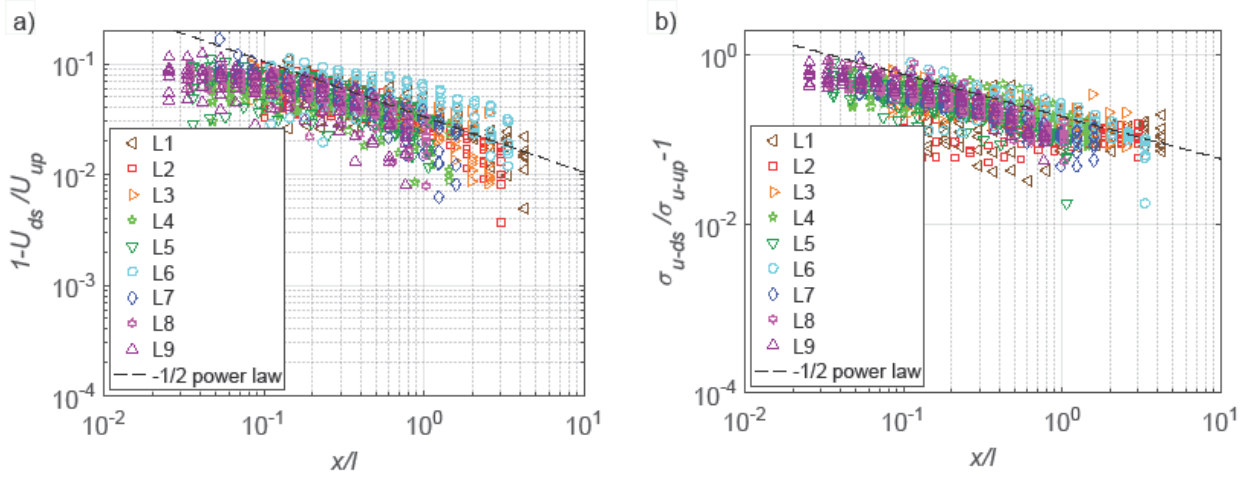
12

Fig. 6 The effects of blade models on the longitudinal velocity in relation to (a) mean value and (b) standard deviation. In both plots, the -1/2 slope line is shown as the data suggest that the effects of blade models on the flow diminish following this slope for $x/l > 0.1$. The distance x from the blade free end is normalised using the blade length l. All flow scenarios are shown

Similarly to what is reported for σ_u, the turbulence intensity T_i attains increased values in the vicinity of the free end of seaweed blade models, and then T_i decreases as the distance from the free end grows. Close to the blade free end, T_i is up to 100% higher compared to the upstream values in front of the blade ($T_{i-up} = 5\% - 6\%$), this increase is reduced to 20% at the furthest measurement point behind the blade. Interestingly, the turbulence intensity shows the highest growths for the flow scenarios characterised by low mean velocities. Effects of seaweed blade models on the skewness and kurtosis of the longitudinal velocity in the wake are not as significant as those reported for U and σ_u and no general trends are identified.

To better understand the turbulence enhancement in the wake of blades, the pre-multiplied spectra $fS_u(f)$ of the longitudinal velocity were analysed. These quantities are advantageous over conventional spectra $S_u(f)$ as they emphasise secondary spectral peaks occurring at high frequencies. Furthermore, the pre-multiplied spectra are dimensionally equivalent to specific energy (e.g. mm²/s² in Fig. 7), making them appropriate tools for investigating the variations in turbulent energy. The pre-multiplied spectra reveal that turbulence is enhanced within a well-defined range of frequencies, which is consistent among the seaweed blade models, but depends upon the flow scenarios. Turbulence enhancement is well-visible for flow scenarios 'Run 1', 'Run 2', and 'Run 3'. With increase in the mean flow velocity, the enhancement region moves to higher frequencies. This trend can be seen comparing Fig. 7a, showing the pre-multiplied spectrum of the longitudinal velocity for flow scenario 'Run 1', and Fig. 7b, representing flow scenario 'Run 3' (both plots refer to seaweed blade model 'L7'). Since Taylor's hypothesis of frozen turbulence was found to be approximately valid for the cases investigated [53], the frequency domain can be converted into the wavenumber domain. This transformation reveals that the turbulence enhancement is localised in a well-defined range of length scales between 0.01 m and 0.1 m (Fig. 7c, d). The turbulent fluctuations contributing to this scale range are likely the result of interactions between the flow and seaweed blade models leading to vortex shedding. In the present study, vortices are shed from the free end of blade models and, in turn, affect the blade models reconfiguration (section 3.2).
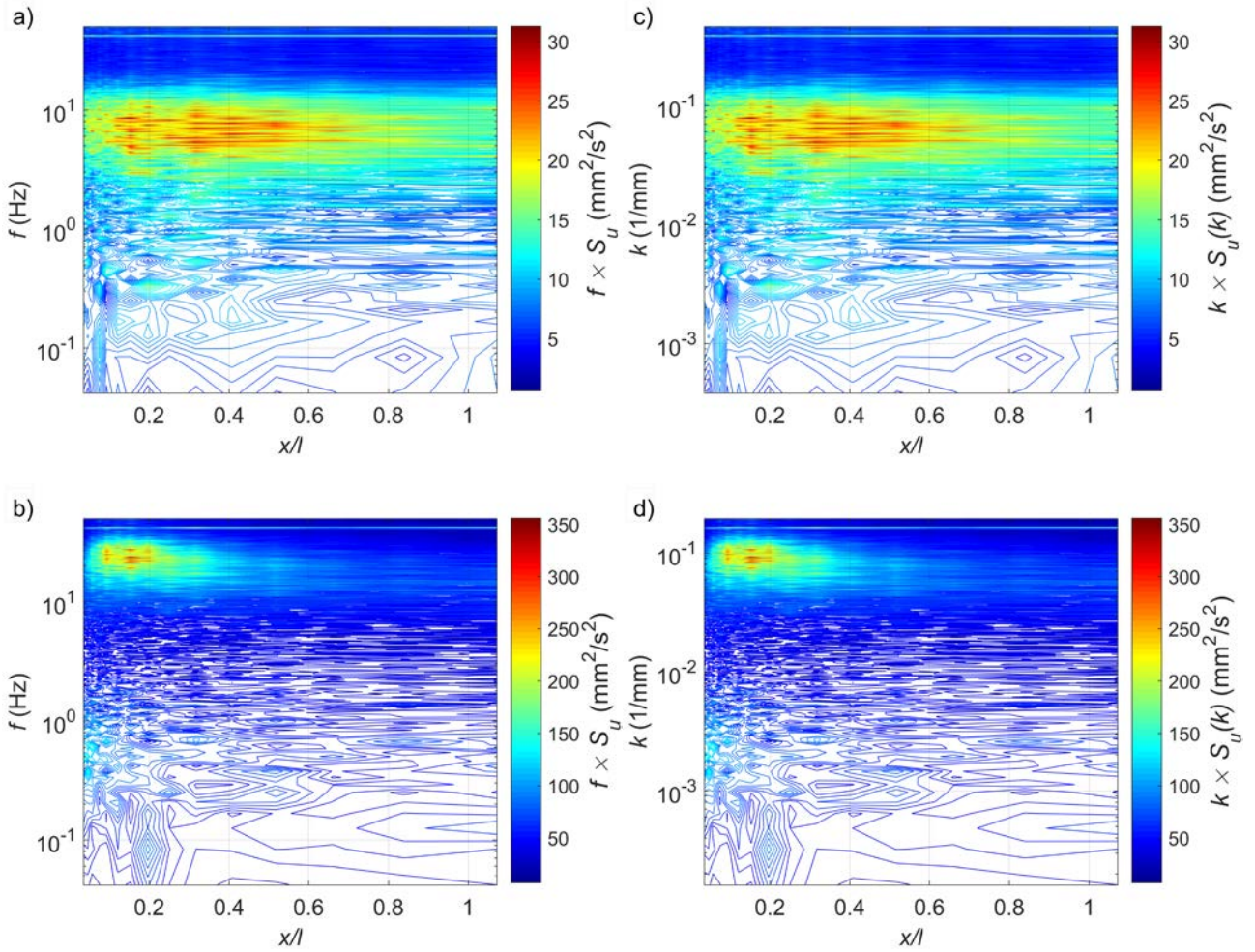
Fig. 7 Pre-multiplied spectra of the longitudinal velocity in the wake of seaweed blade model 'L7' as a function of the frequency and wavenumber: (a, c) flow scenario 'Run 1', (b, d) and flow scenario 'Run 3'. Comparing (a) and (b) it is apparent that the region within which turbulence enhancement occurs moves to higher frequencies as the mean flow velocity increases. In (a) and (b) the pre-multiplied spectra are computed as the magnitude of the longitudinal velocity spectrum times the frequency; in (c) and (d) they are computed as the magnitude of the wavenumber spectrum times the wavenumber. The distance x from the blade free end is normalized using the blade length l

3.4. Coupling between turbulence, drag force and blade reconfiguration (single blades case)
This section reports on the coupling between turbulence, drag force, and blade reconfiguration identified using ordinary coherence functions, which are helpful tools to gain insight into the link between two time series. The ordinary coherence function between two time series $a(t)$ and $b(t)$ is defined as [3]:

$$\gamma^2{}_{a-b} = |S_{ab}(f)|^2/[S_a(f)S_b(f)] \tag{9}$$

where $S_{ab}(f)$ is the cross-spectrum, $S_a(f)$ and $S_b(f)$ are the spectra of the time series $a(t)$ and $b(t)$, respectively. The most significant outcomes of coherence function analysis relate to: (i) the relation between the longitudinal velocity and drag force; (ii) the effect of the vertical velocity on the blade reconfiguration; and (iii) the connection between the drag force and blade reconfiguration.

As the mean flow velocity increases, so do the spectral magnitudes of the longitudinal velocity (Fig. 8a) and drag force (Fig. 8b). From the analysis of the ordinary coherence functions $\gamma^2{}_{u-d}$ between them (Fig. 8c) it is evident that drag fluctuations are passive reflections of fluctuations in the approach longitudinal velocity within a range of low frequencies up to 1 Hz. Indeed, the ordinary coherence functions display high values within the lower range of frequencies, followed by a steep

14

drop in the coherence function levels at higher frequencies (Fig. 8c). As the mean flow velocity increases, the values of γ^2_{u-d} at low frequencies grow, reaching a maximum between 0.9 and 1.0, while the frequency range over which the approach velocity and drag are significantly correlated widens towards higher frequencies. These trends are well visible at low flow rates (i.e. 'Run 1' to 'Run 4'), whereas at higher flow rates no variation in the coherence function shape is noticeable. Fluctuations of w_b at a blade free end are found to strongly correlate with fluctuations of the approach vertical velocity w_{up} as the coherence function γ^2_{w-wb} between them is above the significance level for a broad range of frequencies (Fig. 8f). As the flow velocity grows, γ^2_{w-wb} increases and the range of frequencies over which it is significant widens.
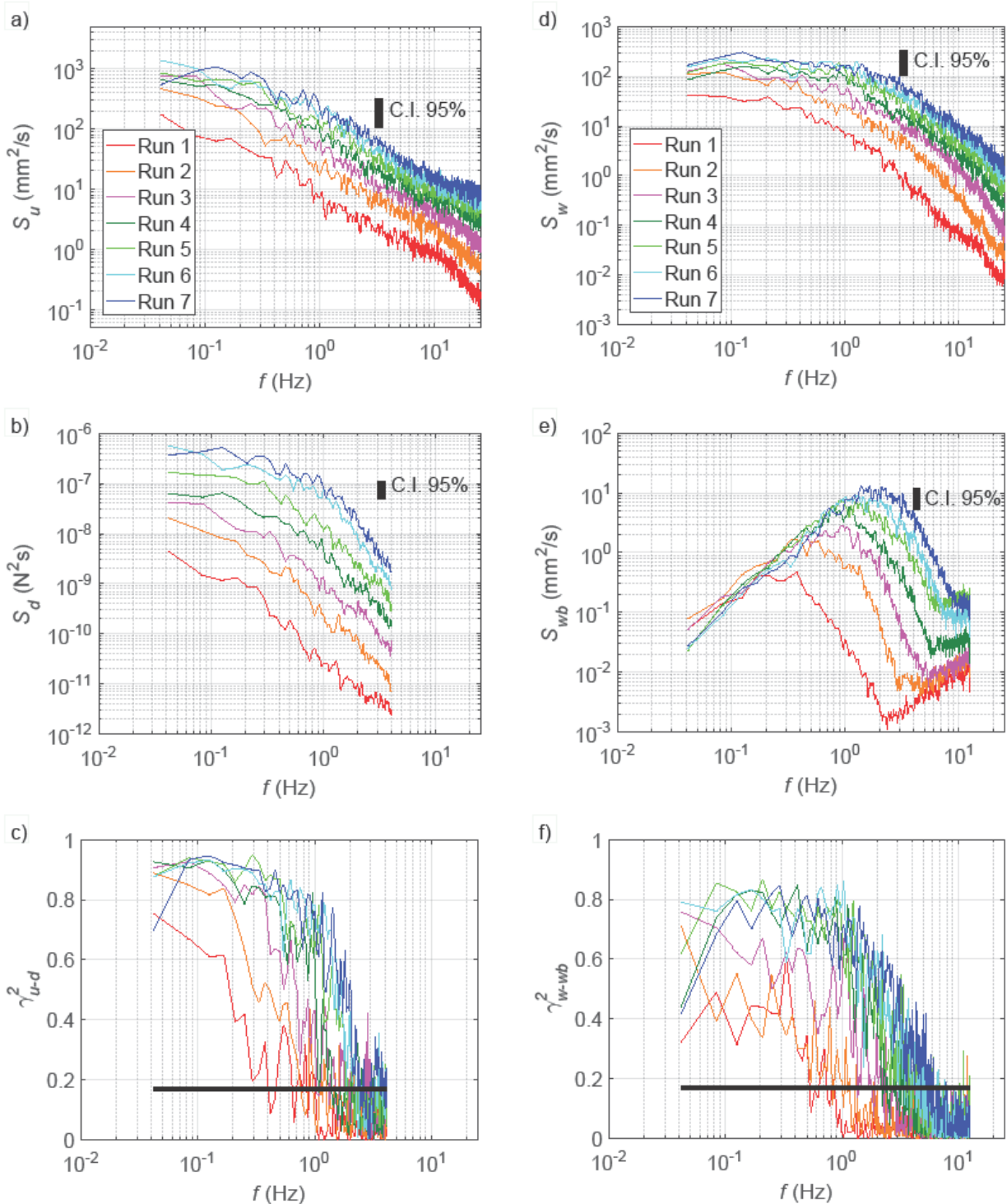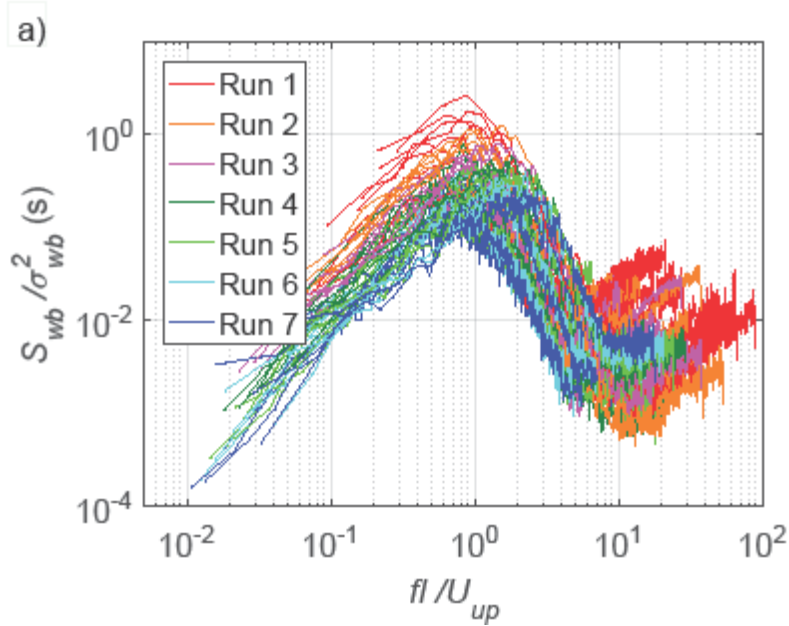
Fig. 8 Spectra of (a) approach longitudinal velocity, (b) drag force, and (c) coherence functions between them; spectra of (d) approach vertical velocity, (e) blade vertical velocity, and (f) coherence functions between them. The thick black lines in (c) and (f) represent 1% significance level of the coherence functions computed according to Shumway and Stoffer [44]. The data relate to model 'L3' (Table 2), and the patterns displayed are representative of all blade models

In Fig. 9a, the obtained $S_{wb}(f)$ are normalised with the variance of w_b while the frequency is normalised with U_{up}/l. So normalised frequency represents, essentially, the ratio of the blade length l to the eddy length scale L, i.e. $fl/U_{up} = l/L$, $L = U_{up}/f = U_{up}T$, $f = 1/T$. All studied scenarios follow a common general trend, exhibiting a high 'hill' at the intermediate frequencies at around $fl/U_{up} = 0.3 - 2$ and with the spectra decreasing on both sides of this region (i.e. for lower and higher frequencies). These results suggest that turbulent eddies in the range between $0.5l$ and $3l$ are most efficient in controlling blade motions. Within the high frequency region, the normalised spectra exhibit stronger differentiation of spectral curves corresponding to different flow scenarios. In particular, flow scenarios characterised by low mean flow velocity display higher spectral magnitude within this region. The correlation between ambient turbulence and drag force is further examined analysing γ^2_{u-d} as a function of the ratio of blade length to eddy length scale (Fig. 9b). The coherence functions are close to unity in the range of $fl/U_{up} < 0.2$ and show a decrease as fl/U_{up} increases, losing significance at around $fl/U_{up} = 0.5$. Some localised peaks are visible at higher frequencies; they are generated as a consequence of the apparently random peaks present in the spectra of drag force (see Fig. 4). Therefore, the obtained results indicate that drag fluctuations in blade models are mainly induced by eddies much larger than the blade length.
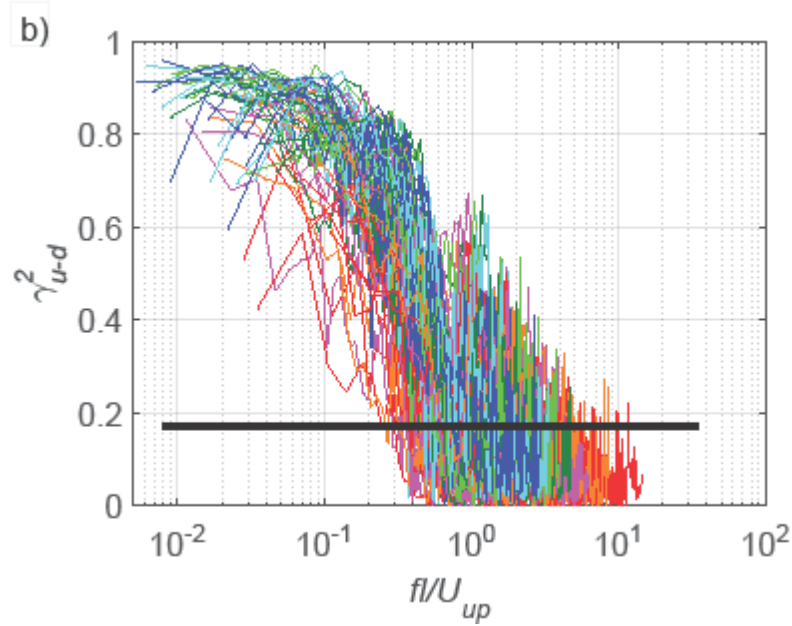
Fig. 9 (a) Spectra of blade vertical velocity (normalised by its variance) as a function of the ratio of the blade length to the eddy length scale. (b) Ordinary coherence functions between longitudinal velocity of the approach flow and drag force as a function of the ratio of the blade length to the eddy length scale. Data for all flow scenarios and blade models are shown

Differently from the coupling between flow and blade velocities, the correlations between blade vertical velocity and drag force are not as profound. Fluctuations of the drag force do not seem to be strongly connected to those of the vertical position or velocity of blades.

3.5. Propagation of blade model oscillations

The propagation of oscillations of seaweed blade models is analysed using a technique based on the cross-correlation between the vertical positions of centroids at two locations (section 2.5; for a full description see [53]). The optimal configuration requires the locations to be selected in the middle of the blade and approximately $0.25l$ apart. The time required for propagation of oscillations of the blade vertical positions from the upstream location to a downstream location is obtained as the time lag corresponding to the maximum value of the cross-correlation between motions of the blade at these two locations. The propagation velocity V_P of oscillations is then estimated as the ratio of the distance between the upstream and downstream locations to the propagation time. In addition, the wavelength L_p of oscillations is evaluated as a product of V_P and the integral time scale T_p of oscillations obtained from integration of the autocorrelation function of the vertical position of the centroid at the centre of the considered section.

The computed propagation velocity V_p of oscillations is between $0.8U_{up}$ and $3U_{up}$, with most values lower than $1.5U_{up}$. Results indicate that the ratio V_p/U_{up} tends asymptotically to 1.0 as the blade Reynolds number Re_l increases (Fig. 10a). A similar trend is also found considering a dependence of V_p/U_{up} on the Cauchy number C_y. At high Re_l and C_y, oscillations move along the blade with a flow speed as travelling waves, independently of the blade properties. The wavelength L_p of oscillations varies from $0.4l$ to $2.5l$ and asymptotically tends to $0.5l$ as Re_l and C_y grow. Interestingly, V_p and L_p appear to be (quasi) linearly dependent once normalised using the mean approach velocity U_{up} and the blade length l (Fig. 10b).
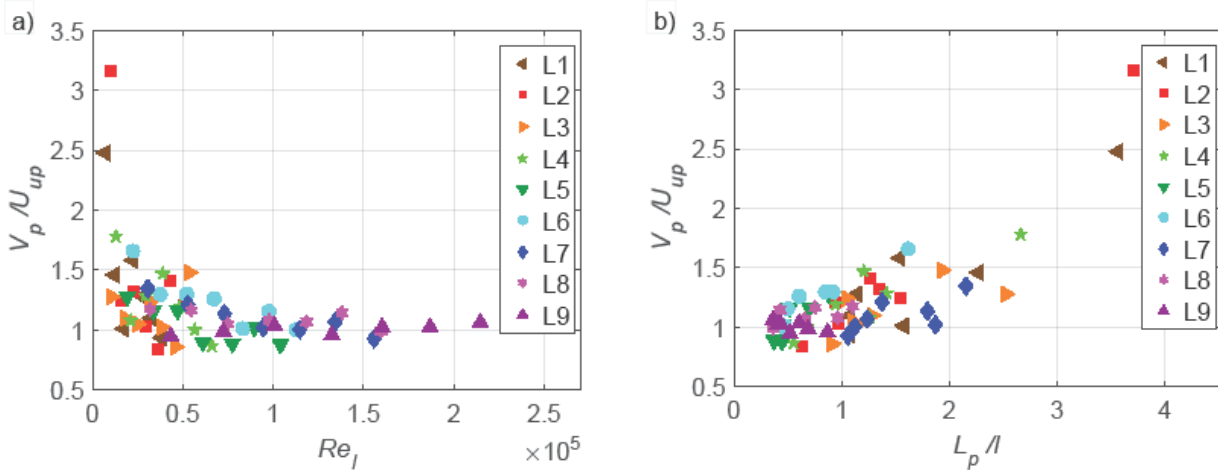
Fig. 10 Dependence of the oscillation propagation velocity V_p (normalised using the mean approach velocity) on the blade Reynolds number (a) and the oscillation wavelength L_p normalised using the blade length (b). Data for all flow scenarios are shown

3.6. Drag force experienced by pairs of blade models

As was noted in section 2.3.2, the experiments with pairs of blade models were conducted for a limited number of scenarios compared to those for single isolated blade models (Table 3). The estimation of C_d for the downstream blade would require velocity data from the wake of the upstream blade. Since this information is not available, the mean drag force is used as a parameter to study potential effects of blades interference. The data show that the sum of the mean drag forces experienced by the pair of blades (referred to as total drag force in the following) is not significantly influenced by the separation Δx between them, if the separation does not exceed two blade lengths (i.e. the range investigated in this work). It is evident that the upstream blade always experiences a higher mean drag force compared to the downstream blade in its wake (Fig. 11a, b). The difference between the mean drag forces is higher at low mean flow velocity ('Run 1P') and is less significant at high flow velocity ('Run 2P'). Depending on the characteristics of the seaweed blade models, different trends are identified. The total drag experienced by blade models 'L1' (short blades) is more than the double mean drag force F_{d-ref} of a single (isolated) blade model (Fig. 11a), while the opposite is seen for blade models 'L7' (long blades, Fig. 11b), regardless of the flow scenario.
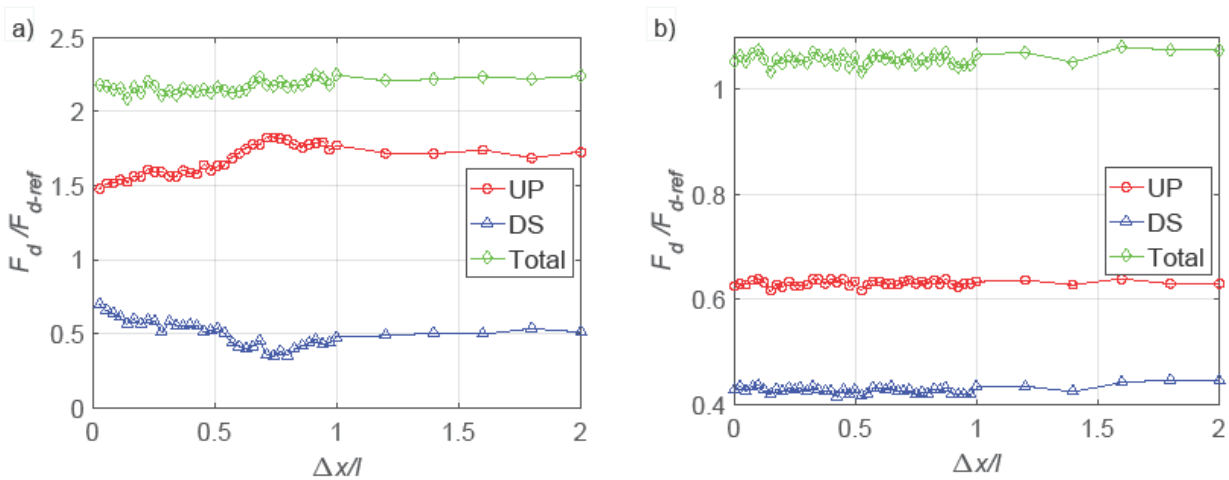

Fig. 11 Normalised mean drag force of a pair of blade models as a function of the nondimensional separation $\Delta x/l$ between the blades: (a) scenario 'L1 Run 1P'; (b) scenario 'L7 Run 1P'. The plots display the normalised mean drag force experienced by the upstream blade ('UP'), the downstream blade ('DS') and the sum of these two quantities ('Total'); the patterns displayed in (a) and (b) are representative of flow scenario 'Run 2P' as well. Normalisation is achieved using the mean drag force F_{d-ref} experienced by a single (isolated) blade model at the same hydraulic conditions

18

4. Discussion

Dynamics of seaweed blade models appear to be mainly controlled by turbulent fluctuations of flow velocities, the most significant of which are fluctuations of w_{up}. The standard deviation of the blade vertical velocity increases along the blade and with the mean flow velocity, similar to what was reported by Cameron et al. [7] and Siniscalchi and Nikora [46] for freshwater macrophytes. As the mean flow velocity increases, it induces: (i) growth in the amplitude of blade model oscillations (Fig. 5a); (ii) shift of the region of maximum magnitude of $S_{wb}(f)$ towards higher frequency (Fig. 5b); and (iii) reduction of auto-correlation of blade reconfiguration. Also, the results of spectral analysis of vertical velocities of flow and seaweed blade model and their ordinary coherence functions (Fig. 8d-f) indicate an important role of turbulence in the dynamics of blade models, revealing that the most energetic region of $S_{wb}(f)$ (i.e. medium frequencies) is controlled by turbulence of the approach flow. A '-4' scaling region that links the maximum peak to the noise floor identified in $S_{wb}(f)$ (Fig. 5b) may reflect the mechanisms that dampen blade oscillations associated with vortices with wavelength smaller than the blade length (Fig. 9a). In addition, the normalised spectra of blade vertical velocity exhibit a high 'hill' at the intermediate frequencies at around $fl/U_{up} = 1$, suggesting that turbulent eddies in the range between 0.5l and 3l are most efficient in controlling blade motions (Fig. 9a). Interestingly, the wavelengths L_p of oscillations on seaweed blade models (Fig. 10b) are consistent with the length scales of the most effective eddies driving blade motions. The relative wavelengths of blade oscillations are also consistent with findings on the wavelength of body fluctuations reported by Barrett et al. [2] and Connell and Yue [12] for fish and slender bodies.

From the analysis of ordinary coherence functions and cross-correlation functions, the drag force experienced by seaweed blade models does not appear to be correlated significantly with the reconfiguration of the blades. Therefore, the pressure drag is assumed to be much smaller than the viscous drag that seems to be dominant. The ordinary coherence functions γ^2_{u-d} show that the drag fluctuations are strongly correlated with the turbulence in the approach flow at low frequencies (Fig. 8c). The spectra of the drag force exhibit '-1' and '-5/2' scaling regions (Fig. 4), consistent with previous studies and hinting at some kind of 'universality'. It is suggested that each region in $S_d(f)$ is descriptive of the key mechanisms involved, i.e.: (i) the '-1' scaling region (low frequency range) reflects a passive interaction between the flow and the blade, with the magnitude of $S_d(f)$ being influenced only by the flow velocity and the blade surface area; and (ii) the '-5/2' scaling region (high frequency range) is the result of the dynamic interactions between the flow and the blade, resulting in a stronger damping effect on drag fluctuations. Analysing γ^2_{u-d} as a function of fl/U_{up}, these regions can be better identified for all cases investigated (Fig. 9b): fluctuations in drag force are controlled by turbulent fluctuations of u_{up} for eddies much larger than the blade (i.e. $L_u > 5l$), while they are dampened for smaller eddies. These findings are similar to the results of Plew et al. [37], who reported a coherent interaction between a freshwater macrophyte within a canopy and turbulent structures for eddies bigger than twice the size of the macrophyte. While Plew et al. [37] focused on the drag force experienced by a macrophyte, in the present study blade dynamics is characterised considering both drag force and reconfiguration. Results shown in Fig. 9 suggest a trade-off in the interactions between flow turbulence and dynamics of seaweed blade models. Vortices much bigger than the blades induce strong drag fluctuations (Fig. 9b) as the blades are not able to comply with them, which is reflected in low amplitude of blade oscillations at small values of fl/U_{up} (Fig. 9a). Vortices with length scale similar to blade length induce larger oscillations in the blades and weak drag fluctuations. As the vortices become smaller compared to blades (i.e. high values of fl/U_{up}), they become more and more unable to drive blade dynamics making correlations between drag force and blade vertical velocity insignificant (Fig. 9b).

It is interesting that the $S_d(f)$ of short blades (i.e. 'L1' and 'L2') at low velocity conditions do not show the '-5/2' scaling region (Fig. 4a). The drag coefficients of these blades appear to follow a

trend that differs from all other blades in the relationship of C_d vs C_y (Fig. 3d). It is likely that this inconsistency is associated with the ratio of the blade length to the integral turbulence length scale l/L_u (Fig. 3b), which may be used as a parameter for describing the length scale of the dominant vortices in the flow. Indeed, the drag coefficient decreases significantly as l/L_u increases, with the highest values of C_d, corresponding to models 'L1' and 'L2', at $l/L_u < 1.0$ (Fig. 3b). This indicates that when seaweed blade models cannot be compliant with the dominant eddies in the flow, they are characterised by higher drag coefficients. The importance of turbulence in characterising the drag coefficient of blade models is also supported by the tendency of C_d to increase with increase in the turbulence intensity (Fig. 3c). In studies of fish locomotion (e.g. [2, 27]), drag reduction was found to be associated with a propagation velocity of oscillations equal to or greater than the mean longitudinal velocity of the flow. However, no clear correlation between drag and propagation velocity of oscillations is found in the present study.

In general, as reported in some works (e.g., [4, 56]), plants decrease their drag coefficient as the mean flow velocity grows via a number of mechanisms. The effectiveness of these mechanisms can be assessed through Vogel's exponent γ [56], which is the value to add to the exponent of 2 of the mean longitudinal velocity, i.e. $F_d \sim U^{2+\gamma}$. Recalling Eq. 8 it is clear that non-zero γ emerges as a result of the dependence of the drag coefficient and blade reference area on the approach velocity. Plants reduce drag via reconfiguration, which can be seen as a combination of static (i.e. plant posture) and dynamic (e.g. flapping) components. The drag reduction reported for most studied plant species is therefore associated with negative values of γ. For example, Buck and Buchholz [6] for samples of *S. latissima* estimated values of γ from -0.7 to -0.4. Considering the posture of seaweed blades (i.e. parallel to the flow), it is clear that they can achieve drag reduction only via dynamic reconfiguration. In the present study, γ varies from -0.6 to 0.2, with positive values associated with long seaweed blade models (i.e. 'L8', and 'L9'), which do not experience drag reduction. This result is consistent with the drag coefficient increasing as a function of the Cauchy number for values of C_y greater than 10^4 (Fig. 3d) and with the results reported by Rominger and Nepf [39] for seaweed blade models in a vortex street.

A deformable body at specific flow conditions experiences the minimum drag force when its projected frontal area is minimised, which generally occurs at high mean flow velocities. However, higher mean velocities are typically associated with stronger fluctuations of instantaneous velocities. As these fluctuations increase, so do the fluctuations of drag and lift forces exerted by the flow on the body. When they become strong enough, fluctuations of flow velocities cause wide oscillations in the body, increasing its projected frontal area and, thus, its drag coefficient (e.g. [21, 43, 55]). Consequently, we suggest that there exists an intermediate region of the Cauchy number where the drag coefficient is minimised. A conceptual picture of the relationship $C_d = f(C_y)$ for a wide range of the Cauchy number values is proposed in Fig. 12, which defines a range of expected survival for submerged aquatic vegetation.
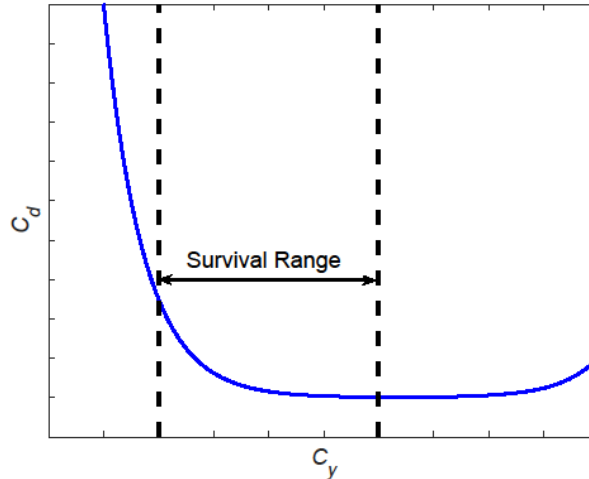
a)

Fig. 12 Conceptual picture for the dependence of the drag coefficient on the Cauchy number showing the expected survival range for submerged aquatic vegetation. Submerged aquatic vegetation is expected to show values of the Cauchy number within an intermediate range in order to avoid, on the one hand, high pressure drag (low Cauchy numbers) and, on the other hand, ample body fluctuations that can lead to dangerous increase in the frontal projected area (and consequent increase in the drag force) at high flow velocity conditions (high Cauchy numbers)

Seaweed blade models have significant effects on the flow characteristics in the downstream wakes, decreasing the mean value and enhancing the standard deviation of the longitudinal flow velocity (Fig. 6a, b). Interestingly, the deviations of both mean and standard deviation from the corresponding values of the approach flow decrease along the wake as a power function with exponent of '-1/2' (Fig. 6a, b). Both turbulent kinetic energy and relative turbulence intensity T_i are greater in the wake of a blade compared to the approach flow. This enhancement is more significant at low flow conditions, with the spectrum of the longitudinal flow velocity showing a stronger energy input into spectra (Fig. 7a-d). As expected for slender deformable bodies, this energy input occurs at high frequencies and is broadbanded [31], indicating that vortices are shed from the free end of blade models. Turbulence production is fostered by blade models through generation of eddies with length scales bigger than approximately 1 cm. This vortex shedding phenomenon affects blade reconfiguration (see secondary peaks in Fig. 5b) and its effect is visible in Fig. 9a, where the collapse of $S_{wb}(f)/\sigma_{wb}^2$ does not occur at high frequencies. However, the effects of this phenomenon are secondary compared to those of ambient turbulence. The authors are not aware of studies of the wake of a deformable slender body that could provide data for comparison with the present findings.

The effects of seaweed blade models on the wake flow are also important for understanding the drag force experienced by a pair of tandem blade models. The results of the present study suggest that the more significant the effect of the upstream blade on the flow, the higher drag reduction is granted to the downstream blade. Since the velocity of the flow in the wake of a blade is lower than the undisturbed flow velocity, the downstream blade experiences a lower mean drag force compared to the upstream blade. The total drag force of short blades 'L1' is more than twice the mean drag of a single (isolated) blade (Fig. 11a), while long blades 'L7' exhibit significant drag reduction (Fig. 11b). Findings from experiments with pairs of blade models are to be considered in the light of the possible limitations introduced by the shallow conditions in which they were performed (i.e. water depth of 14 cm). During experiments we visually monitored blade models to ascertain that they did not touch the water surface or the flume bed and their reconfiguration was not limited by the water depth. Nevertheless, water depth might have influenced blade models dynamics and the reasons for contradictory patterns in total drag experienced by pairs of blade models remain unclear.

The findings of this study can contribute to the development of numerical models and new farming techniques for improving seaweed aquaculture. The role of turbulence in controlling blade

dynamics and its influence on the drag coefficient suggests that seaweed blades may adapt their length to optimise the trade-off between drag fluctuations and reconfiguration. Findings on the relationship between C_D and l/L_u may explain why seaweed blades grow to be several meters long. In some conditions blades may grow so that $l/L_u \approx 1$ in order to limit the drag forces acting on them and be compliant with the flow. In addition, seaweed blades develop corrugations (e.g. [17, 39]) to increase their flexural rigidity, preventing them from having high Cauchy number and, consequently, higher drag coefficient (see Fig. 12). For seaweed blades to have $l/L_u \approx 1$ may be beneficial also for enhancing reconfiguration, which can lead to a potential increase in light and nutrients availability within a canopy (e.g. [33, 46]). Bearing in mind seaweed growth pattern, it is clear that turbulence characteristics at a site are to be taken into account for the design of novel aquaculture techniques.

Physical models used in this study were developed based on the data on seaweed blades from an exposed site (i.e. [6]), but blades from sheltered sites typically show different characteristics (i.e. they are wider and more ruffled). It is, therefore, unknown if the dynamics of a seaweed blade from a sheltered site are controlled by the same mechanisms. Unfortunately, data of turbulence and blade morphology from field studies are not available yet in the literature for comparison with the results of the present work.

5. Conclusions

One of the most important challenges that researchers in environmental fluid mechanics face is to comprehend flow-vegetation interactions at a relevant range of spatial and temporal scales. For developing this knowledge, the determination of the dominant mechanisms in vegetation hydrodynamics is of utmost importance, together with the identification of the most representative dimensionless quantities. This study investigates the physical interactions between turbulent flow and plastic-made models of blades of the seaweed species *S. latissima* via experiments in a laboratory flume facility, featuring measurements of instantaneous drag force, reconfiguration of the blade models, and flow velocities.

We identified two main mechanisms that control the reconfiguration of seaweed blade models depending upon the range of $l/L = fl/U_{up}$: (i) at low frequencies, blade dynamics are driven by the flow turbulence; and (ii) at high frequencies, blade dynamics are the result of dynamic interactions between the flow and the blade, with a more efficient reduction of fluctuations in the drag force and blade vertical velocity. These two frequency regions are visible in the spectra of both drag force and vertical velocity of the blades. We found that C_d increases as T_i grows, and it decreases with increase in the ratio l/L_u. The drag coefficient reaches the minimum at the intermediate values of C_y around $C_y \approx 10^4$, with an increase at greater values of C_y associated with blade fluttering due to strong flow turbulence. Furthermore, we propose a concept of a plant survival range in the domain of C_y for submerged vegetation (Fig. 12). Seaweed blade models affect the flow characteristics, decreasing the mean longitudinal velocity and enhancing flow turbulence in their wakes. These effects of blade models on the flow are fundamental for understanding the drag force experienced by blade models at larger spatial scales.

Despite the progress of this work and other recent studies, the development of novel aquaculture techniques remains limited by the lack of: (i) information at larger spatial scales (i.e. canopy/patch, and farm scales); and (ii) multidisciplinary studies that include measurements of physical and biological parameters to assess seaweed productivity. These two issues have to be addressed in the future studies.

References

1. Albayrak I, Nikora V, Miler O, O'Hare M (2012) Flow-plant interactions at a leaf scale: effects of leaf shape, serration, roughness and flexural rigidity. Aquat Sci 74(2):267-286
2. Barrett DS, Triantafyllou MS, Yue DKP, Grosenbaugh MA, Wolfgang MJ (1999) Drag reduction in fish-like locomotion. J Fluid Mech 392:183-212
3. Bendat JS, Piersol AG (2011) Random data: analysis and measurement procedures. John Wiley and Sons, New Jersey
4. Boller ML, Carrington E (2006) The hydrodynamic effects of shape and size change during reconfiguration of a flexible macroalga. J Exp Bio 209(10):1894-1903
5. Boller ML, Carrington E (2007) Interspecific comparison of hydrodynamic performance and structural properties among intertidal macroalgae. J Exp Bio 210(11):1874-1884
6. Buck BH, Buchholz CM (2005) Response of offshore cultivated *Laminaria saccharina* to hydrodynamic forcing in the North Sea. Aquaculture 250(3):674-691
7. Cameron SM, Nikora VI, Albayrak I, Miler O, Stewart M, Siniscalchi F (2013) Interactions between aquatic plants and turbulent flow: a field study using stereoscopic PIV. J Fluid Mech 732:345-372
8. Canny J (1986) A computational approach to edge detection. IEEE T Pattern Anal 6:679-698
9. Cea L, Puertas J, Pena L (2007) Velocity measurements on highly turbulent free surface flow using ADV. Exp Fluids 42(3):333-348
10. Chan CX, Ho CL, Phang SM (2006) Trends in seaweed research. Trends in Plant Sci 11(4):165-166
11. Chopin T, Sawhney M (2009) Seaweeds and their mariculture. In: Steele (ed) The Encyclopedia of Ocean Sciences, 2nd edn. Academic Press, London, pp 4477-4487
12. Connell BS, Yue DK (2007) Flapping dynamics of a flag in a uniform stream. J Fluid Mech 581:33-67
13. de Langre E (2008) Effects of wind on plants. Annu Rev Fluid Mech 40:141-168
14. Fei X (2004) Solving the coastal eutrophication problem by large scale seaweed cultivation. Hydrobiologia 512(1-3):145-151
15. Frostick LE, McLelland SJ, Mercer TG (2011) Users Guide to Physical Modelling and Experimentation: Experience of the HYDRALAB Network. CRC Press, Florida
16. Frostick LE, Thomas RE, Johnson MF, Rice SP, McLelland SJ (2014) Users Guide to Ecohydraulic Modelling and Experimentation. CRC Press, Florida
17. Fryer M, Terwagne D, Reis PM, Nepf H (2015) Fabrication of flexible blade models from a silicone-based polymer to test the effect of surface corrugations on drag and blade motion. Limnology and Oceanography: Methods, 13(11):630-639
18. Gaylord B, Denny M (1997) Flow and flexibility. I. Effects of size, shape and stiffness in determining wave forces on the stipitate kelps *Eisenia arborea* and *Pterygophora californica*. J Exp Bio 200(24):3141-3164
19. Gaylord B, Hale BB, Denny MW (2001) Consequences of transient fluid forces for compliant benthic organisms. J Exp Bio 204(7):1347-1360
20. Goring DG, Nikora VI (2002) Despiking acoustic Doppler velocimeter data. J Hydraul Eng ASCE 128(1):117-126
21. Hoerner SF (1965) Fluid-dynamic drag: practical information on aerodynamic drag and hydrodynamic resistance. Hoerner Fluid Dynamics, New Jersey
22. Huang I, Rominger JT, Nepf H (2011) The motion of kelp blades and the surface renewal model. Limnol Oceanogr 56(4):1453–1462
23. Hughes AD, Kelly MS, Black KD, Stanley MS (2012) Biogas from macroalgae: is it time to revisit the idea. Biotechnol Biofuels 5(86):1-7
24. Hurther D, Lemmin U (2001) A correction method for turbulence measurements with a 3D acoustic Doppler velocity profiler. J Atmos Ocean Tech 18(3):446-458

25. Jesson M, Sterling M, Bridgeman J (2013) Despiking velocity time-series—Optimisation through the combination of spike detection and replacement methods. Flow Meas Instrum 30:45-51

26. Koehl MAR (2003) Physical modelling in biomechanics. Philos T Roy Soc B 358(1437):1589-1596

27. Lighthill MJ (1960) Note on the swimming of slender fish. J Fluid Mech 9(02):305-317

28. Lucas JS, Southgate PC (2012) Aquaculture: Farming aquatic animals and plants. Wiley-Blackwell, New Jersey

29. Martienssen W, Warlimont H (2006) Springer handbook of condensed matter and materials data. Springer Science and Business Media, Berlin, pp 477-522

30. Mata L, Schuenhoff A, Santos R. (2010). A direct comparison of the performance of the seaweed biofilters, *Asparagopsis armata* and *Ulva rigida*. J Appl Phycol 22(5):639-644

31. Nakamura Y, Ohya Y, Tsuruta H. (1991) Experiments on vortex shedding from flat plates with square leading and trailing edges. J Fluid Mech 222:437-447

32. Nikora VI, Goring DG (1998) ADV measurements of turbulence: Can we improve their interpretation?. J Hydraul Eng ASCE 124(6):630-634

33. Nikora V (2010) Hydrodynamics of aquatic ecosystems: an interface between ecology, biomechanics and environmental fluid mechanics. River Res Appl 26(4):367-384

34. Nortek (2004). Vectrino User Guide. Available: www.nortek-as.com/en/support/manuals

35. Parke M (1948) Studies on British Laminariaceae. I. Growth in *Laminaria saccharina* (L.) Lamour. Journal of the Marine Biological Association of the United Kingdom, 27(3):651-709

36. Parsheh M, Sotiropoulos F, Porté-Agel F (2010) Estimation of power spectra of acoustic-Doppler velocimetry data contaminated with intermittent spikes. J Hydraul Eng ASCE 136(6):368-378

37. Plew DR, Cooper GG, Callaghan FM (2008) Turbulence-induced forces in a freshwater macrophyte canopy. Water Resour Res, 44(2)

38. Paul M, Bouma TJ, Amos CL (2012) Wave attenuation by submerged vegetation: combining the effect of organism traits and tidal current. Mar Ecol-Prog Ser 444:31-41

39. Rominger JT, Nepf HM (2014) Effects of blade flexural rigidity on drag force and mass transfer rates in model blades. Limnol Oceanogr 59(6):2028-2041

40. Sánchez-González JF, Sánchez-Rojas V, Memos CD (2011) Wave attenuation due to Posidonia oceanica meadows. J Hydraul Res 49(4):503-514

41. Sanderson JC (2006) Reducing the environmental impact of seacage fish farming through cultivation of seaweed. Doctoral dissertation, The Open University, UK and UHI Millenium Institute

42. Schlichting H, Gersten K (2000) Boundary-layer theory. Springer Science and Business Media, Berlin

43. Shelley MJ, Zhang J (2011) Flapping and bending bodies interacting with fluid flows. Annu Rev Fluid Mech 43:449-465

44. Shumway RH, Stoffer DS (2000) Time series analysis and its applications. Springer, Berlin

45. Siniscalchi F, Nikora VI (2012) Flow-plant interactions in open-channel flows: A comparative analysis of five freshwater plant species. Water Resour Res 48(5)

46. Siniscalchi F, Nikora V (2013) Dynamic reconfiguration of aquatic plants and its interrelations with upstream turbulence and drag forces. J Hydraul Res 51(1):46-55

47. Spurkland T, Iken K (2012) Seasonal growth patterns of *Saccharina latissima* (Phaeophyceae, Ochrophyta) in a glacially-influenced subarctic estuary. Phycol Res 60(4):261-275

48. Statzner B, Lamouroux N, Nikora V, Sagnes P (2006) The debate about drag and reconfiguration of freshwater macrophytes: comparing results obtained by three recently discussed approaches. Freshwater Biol 51(11):2173-2183

49. Temmerman S, Meire P, Bouma TJ, Herman PMJ, Ysebaert T, De Vriend HJ (2013) Ecosystem-based coastal defence in face of global change. Nature 504:79-83

50. Thomas RE, Johnson MF, Frostick LE, Parsons DR, Bouma TJ, Dijkstra JT, McLelland SJ, Moulin FY, Myrhaug D, Neyts A, Paul M, Penning WE, Puijalon S, Rice SP, Stanica A, Tagliapietra D, Tal M, Tørum A, Vousdoukas M (2014). Physical modelling of water, fauna and flora: knowledge gaps, avenues for future research and infrastructural needs. Journal of Hydraulic Research, 52(3), 311-325

51. Thomson J, Polagye B, Richmond M, and Durgesh V (2010) Quantifying turbulence for tidal power applications. In: Proc. OCEANS 2010, Seattle, WA, 20–23 September 2010. IEEE, New York, NY, pp 1-8

52. Thomson J, Polagye B, Durgesh V, Richmond MC (2012) Measurements of turbulence at two tidal energy sites in Puget Sound, WA. IEEE Journal of Oceanic Engineering, 37(3):363-374

53. Vettori D (2016) Hydrodynamic performance of seaweed farms: an experimental study at seaweed blade scale. Doctoral dissertation, University of Aberdeen

54. Vettori D, Nikora V (2017) Morphological and mechanical properties of blades of *Sacchartna latissima*. Estuar Coast Shelf S 196:1-9

55. Vogel S (1989) Drag and reconfiguration of broad leaves in high winds. J Exp Bot 40(8):941-948

56. Vogel S. (1994) Life in moving fluids: the physical biology of flow. Princeton University Press, Massachusetts

57. Wargacki AJ, Leonard E, Win MN, Regitsky DD, Santos CNS, Kim PB, Cooper SR, Raisner RM, Herman A, Sivitz AB, Lakshmanaswamy A, Kashiyama Y, Baker D, Yoshikuni Y (2012) An engineered microbial platform for direct biofuel production from brown macroalgae. Science 335(6066):308-313